

**Key Points:**

- Experiments show 2D dune pattern coarsening from a thin sediment bed through dune-dune interactions
- Bedform amplitude and wavelength display exponentially saturated growth
- Combining experiments with Large Eddy Simulations finds a power-law relation between the friction velocity and the initial growth rate

**Supporting Information:**

Supporting Information may be found in the online version of this article.

**Correspondence to:**

P. A. Jarvis,  
p.jarvis@gns.cri.nz

**Citation:**

Jarvis, P. A., Bacik, K. A., Narteau, C., & Vriend, N. M. (2022). Coarsening dynamics of 2D subaqueous dunes. *Journal of Geophysical Research: Earth Surface*, 127, e2021JF006492. <https://doi.org/10.1029/2021JF006492>

Received 19 OCT 2021

Accepted 30 JAN 2022

**Author Contributions:**

**Conceptualization:** N. M. Vriend

**Formal analysis:** P. A. Jarvis, K. A. Bacik

**Funding acquisition:** N. M. Vriend

**Investigation:** P. A. Jarvis, K. A. Bacik

**Methodology:** P. A. Jarvis, K. A. Bacik, N. M. Vriend

**Project Administration:** N. M. Vriend

**Resources:** N. M. Vriend

**Software:** C. Narteau

**Supervision:** C. Narteau, N. M. Vriend

**Writing – original draft:** P. A. Jarvis

**Writing – review & editing:** P. A. Jarvis, K. A. Bacik, C. Narteau, N. M. Vriend

<sup>1</sup>Department of Applied Mathematics and Theoretical Physics, University of Cambridge, Cambridge, UK, <sup>2</sup>Department of Earth Sciences, University of Geneva, Geneva, Switzerland, <sup>3</sup>Wairakei Research Centre, GNS Science, Taupo, New Zealand, <sup>4</sup>Department of Mathematical Sciences, Centre for Networks and Collective Behaviour, University of Bath, Bath, UK, <sup>5</sup>Institut de Physique du Globe de Paris, Sorbonne Paris Cité, Université Paris Diderot, Paris, France, <sup>6</sup>BP Institute, University of Cambridge, Cambridge, UK, <sup>7</sup>Department of Earth Sciences, University of Cambridge, Cambridge, UK

**Abstract** Fluid flow over an initially flat granular bed leads to the formation of a surface-wave instability. The sediment bed profile coarsens and increases in amplitude and wavelength as disturbances develop from ripples into dunes. We perform experiments and numerical simulations to quantify both the temporal evolution of bed properties and the relationship between the initial growth rate and the friction velocity  $u_*$ . Experimentally, we study underwater bedforms originating from a thin horizontal particle layer in a narrow and counter-rotating annular flume. We investigate the role of flow speed, flow depth and initial bed thickness on dune evolution. Bedforms evolve from small, irregular disturbances on the bed surface to rapidly growing connected terraces (2D equivalent of transverse dunes) before splitting into discrete dunes. Throughout much of this process, growth is controlled by dune collisions which are observed to result in either coalescence or ejection (mass exchange). We quantify the coarsening process by tracking the temporal evolution of the bed amplitude and wavelength. Additionally, we perform Large Eddy Simulations (LES) of the fluid flow inside the flume to relate the experimental conditions to  $u_*$ . By combining the experimental observations with the LES results, we find that the initial dune growth rate scales approximately as  $u_*^5$ . These results can motivate models of finite-amplitude dune growth from thin sediment layers that are important in both natural and industrial settings.

**Plain Language Summary** If the flow of water over a flat bed of sand is sufficiently fast, then grains of sand can be picked up, transported and deposited to form sand dunes. Initially, many small dunes form but, as the flow continues, they grow and merge to become a smaller number of larger dunes. We have performed experiments investigating the formation and growth of underwater dunes from an initially flat bed of sediment. In particular, we vary the speed of the flow, the depth of the water and the thickness of the sediment bed. We observe that the dunes initially grow rapidly, before reaching an almost-constant height that increases with the sediment thickness. In order to relate the initial dune growth rate to the driving flow, we have also performed numerical simulations of the water flow in the experiment. This enables us to better-constrain the shear stress on the sediment bed, which is quantified through the friction velocity  $u_*$ . By combining the experimental and numerical results, we show that the initial dune growth rate is approximately proportional to  $u_*^5$ . These results can form a starting point for models describing the growth of underwater dunes.

### 1. Introduction

Bedforms create self-organizing patterns, from wind-blown dunes on Earth and other planets (Lorenz & Zimbelman, 2014; Telfer et al., 2018) to ripples on riverbeds or beaches (Best, 1995). In industry, sedimenting particles can block pipes, while bedform formation can hinder multiphase particle-fluid transport in production lines (Florez & Franklin, 2016). In nature, extreme events including floods and tsunamis can drastically alter sedimentary structures on seafloors and river beds, impacting flooding potentials and shipping channels (Barnard, 2006). The associated economic and humanitarian consequences motivate the need to understand the physical behavior of bedforms and predict their temporal evolution.

Dune formation and evolution is a multi-scale phenomenon, occurring when sufficiently strong fluid flow above unconsolidated sediment drives particle erosion and transport (Bagnold, 1941; Salevan et al., 2017; Shields, 1936). Initial instabilities from a flat bed can be modeled as a linear stability problem (Andreotti et al., 2002b; Charru et al., 2013; Colombini & Stocchino, 2011; Fourrière et al., 2010; Gadal et al., 2018) but, as the perturbations grow, nonlinear coarsening, defined as a process whereby many smaller oscillations of the bed surface develop

© 2022. The Authors.

This is an open access article under the terms of the [Creative Commons Attribution License](https://creativecommons.org/licenses/by/4.0/), which permits use, distribution and reproduction in any medium, provided the original work is properly cited.

into fewer larger dunes, ensues, consequently increasing the pattern wavelength (Coleman & Melville, 1994; Colombini & Stocchino, 2008; Fredsøe, 1974; Gao et al., 2015; Ji & Mendoza, 1997; Swanson et al., 2017). Here, we examine the latter process using an experimental set-up uniquely equipped to study nonlinear coarsening. Although pattern coarsening is a generic property of the solutions to the nonlinear sediment transport equations (Csahók et al., 2000; Jerolmack & Mohrig, 2005; Valance, 2011) and despite significant progress (Bradley & Venditti, 2019; Fourrière et al., 2010; Gao et al., 2015; Swanson et al., 2017), the coarsening dynamics of bedforms remain poorly understood. In particular, a quantitative relationship between the dune growth rate and the driving fluid flow remains elusive. Additionally, the majority of studies on dune field coarsening have focused on transport-limited regimes (Coleman & Melville, 1994; Gao et al., 2015), where the equilibrium state of the dune field is determined by flow conditions (Martin & Jerolmack, 2013; Reesink et al., 2018). Conversely, sediment-limited regimes, where bare patches of unerodible material become exposed in dune troughs, are relatively understudied. These questions remain partly due to a lack of quantitative experimental validation of existing theoretical and numerical descriptions.

In this study, we present a combined experimental-numerical investigation on the formation and coarsening of 2D bedforms in sediment-limited conditions, testing the influence of bed thickness, flow depth and basal shear stress on the evolution of both dune amplitude and wavelength. We first review previous studies on dune formation and evolution and compare the use of rectangular and annular flumes in experiments (Section 2). In Section 3, we then present our methodology, including experimental measurements of bedform growth within our counter-rotating, annular flume. Whilst this system enables investigation of the long-time behavior as well as minimising rotating frame effects (see Section 2.2), the moving geometry makes it difficult to perform accurate measurements of the fluid velocity profile. We therefore complement these observations with Large-Eddy Simulations (LES) of the fluid flow inside the flume at the onset of the experiment. By combining these two techniques, we then relate the rate of bedform growth to the initial basal shear stress (Section 4). Finally, we discuss (Section 5) and summarize (Section 6) our findings, noting implications for future research.

## 2. Background

### 2.1. Formation and Interaction

Dune formation results from fluid-driven sediment transport. Such transport only occurs if the combined lift and drag forces exceed the particle weight (Bagnold, 1941; Shields, 1936), a balance quantified through the Shields number

$$\theta = \frac{\tau}{(\rho_p - \rho_f)gd}, \quad (1)$$

where  $\tau$  is the surface shear stress,  $\rho_{p(f)}$  the particle (fluid) density,  $g = 9.81 \text{ m s}^{-2}$  the gravitational acceleration and  $d$  the particle diameter. Classically, transport is thought to occur if  $\theta$  exceeds some critical threshold  $\theta_c$ , estimates of which typically vary from 0.03 to 0.09 (Buffington & Montgomery, 1997). However, this picture may be overly simplistic (Pähtz et al., 2020), as suggested by the lack of a sharp stationary/moving transition (Salevan et al., 2017) and the critical role of turbulent fluctuations and particle inertia on sediment transport (Bacik et al., 2020, 2021; Lavelle & Mojfeld, 1987; Paintal, 1971). The friction velocity  $u_*$  is frequently used to parameterize  $\tau$  through  $u_* = \sqrt{\tau/\rho_f}$ , and will be used in our study to relate the strength of the driving fluid flow to dune growth.

For a sufficiently large surface shear stress, subaqueous bedforms arise due to a hydrodynamic instability, originating from a phase shift between the flow velocity and topography (Colombini & Stocchino, 2011; Fourrière et al., 2010; Jackson & Hunt, 1975). Whilst analytical linear stability models can predict initial growth rates (Colombini & Stocchino, 2008, 2011; Fourrière et al., 2010; Lü et al., 2021), the model assumptions break down once the perturbation amplitude becomes too large and a non-linear coarsening regime commences (Coleman & Melville, 1994; Colombini & Stocchino, 2008; Fredsøe, 1974; Gao et al., 2015; Ji & Mendoza, 1997; Swanson et al., 2017). Connected transverse bedforms develop but these can transform into isolated dunes, separated by a bare surface, if the sediment layer is thin enough. In laterally unconfined geometries, a secondary instability forms 3D barchan dunes (Parteli et al., 2011; Reffet et al., 2010), whilst in narrow channels the dunes remain straight and 2D. It is often reported that the dune migration speed  $c$  scales inversely with dune height  $\mathcal{H}$  ( $c \propto 1/\mathcal{H}$ )

(Southard, 1991), but alternative scalings based on length  $\mathcal{L}$  ( $c \propto 1/\mathcal{L}$ ) (Kroy et al., 2002) or a minimum height  $\mathcal{H}_0$  ( $c \propto 1/(\mathcal{H} + \mathcal{H}_0)$ ) (Andreotti et al., 2002a) have also been proposed.

Since differently sized dunes have differential speeds (Reesink et al., 2018), migrating dunes in a confined channel can interact and collide, resulting in a wide range of possible outcomes (Assis & Franklin, 2020; Durán et al., 2005; Endo et al., 2004; Hersen, 2005). For 2D bedforms, dune collisions have been observed to proceed through two possible mechanisms: coalescence or ejection (Coleman & Melville, 1994; Diniega et al., 2010; Gao et al., 2015). Coalescence, also described as merging, describes the coming together of two dunes to form a single, larger dune (Martin & Jerolmack, 2013; Reesink et al., 2018) while ejection involves mass exchange but preserves both dunes. Specifically, ejection occurs when a larger and slower downstream dune loses mass to a smaller and faster upstream neighbor, shrinks, and accelerates away (Coleman & Melville, 1994; Diniega et al., 2010; Gao et al., 2015). The ejection mechanism has also sometimes been referred to as “passing through” since the initially upstream dune can sometimes appear to pass through its larger downstream neighbor (Martin & Jerolmack, 2013). Coalescence and ejection phenomena can occur as part of a suite of processes that take place as a dune field responds to changes in flow conditions (Reesink et al., 2018). In the context of this study, however, such dune collisions are an important mechanism during the coarsening regime, whereby a large number of smaller dunes interact to become a smaller number of bigger dunes (Coleman & Melville, 1994). Baas (1994) experimentally measured the amplitude and wavelength evolution of an initially flat subaqueous sediment surface and fitted the data to the empirical relations

$$\bar{z} = a_z (1 - e^{-b_z t}), \quad (2)$$

and

$$\lambda = a_\lambda (1 - e^{-b_\lambda t}), \quad (3)$$

respectively, where  $\bar{z}$  is the root-mean-squared amplitude of the bed profile,  $\lambda$  is the wavelength (defined as the mean distance between crests),  $t$  is time and  $a_z$ ,  $b_z$ ,  $a_\lambda$ , and  $b_\lambda$  are fitted constants. This empirical model has since been applied to both subaqueous (Baas, 1999; Bradley & Venditti, 2019; Naqshband et al., 2021; Venditti et al., 2005b) and aeolian (Swanson et al., 2017) dunes, although the precise measures of amplitude and wavelength vary (amplitude: peak-to-peak, root-mean-squared; wavelength: crest-to-crest, mean, or mode from spectral analysis). Recent work has further found that, for larger shear stresses, the time of applicability of this exponentially saturated model can be preceded by a transient linear stage (Bradley & Venditti, 2019). Some authors (Coleman et al., 2005; Nikora & Hicks, 1997), however, have fitted power laws to describe the temporal evolution of  $\bar{z}$  and  $\lambda$ , including Gao et al. (2015) who used cellular automaton simulations to find that both  $\bar{z}$  and  $\lambda$  scale as  $\sim t^{1/3}$  prior to saturation. All of these models considered a sufficiently thick initial layer of sediment, such that an unerodible base was never exposed. This is in contrast to our study, where during experiments the troughs between dunes become sufficiently deep for the flume base to become exposed, leading to discrete, migrating dunes.

## 2.2. Rectangular and Annular Flume Studies

In the laboratory, straight rectangular flumes are often used to investigate the formation and migration of 2D and 3D bedforms under various conditions (Coleman & Melville, 1994; Guy et al., 1966; Martin & Jerolmack, 2013; Naqshband et al., 2017; Robert & Uhlman, 2000; Venditti, 2007). However, sediment is continuously lost at the downstream end and it is difficult to provide the required upstream sediment flux for a balanced steady-state system. Racetrack or recirculating flumes with straight sections can partly address this shortcoming (Baas, 1994, 1999; Groh et al., 2009; Reesink et al., 2018), but the finite length of the straight section prohibits probing of long-term steady-state behavior. Alternatively, annular flumes have been used to study processes including turbidity currents (Sumner et al., 2008; Wei et al., 2017), bed erodibility and resuspension (Amos et al., 1992; Charu et al., 2004; Mouilleron et al., 2009; Skulovich et al., 2017; Widdows et al., 2007) but rotating-frame forces create significant secondary circulation and non-2D sedimentary structures. Whilst bedform dynamics have been investigated in annular flumes (Betat et al., 1999, 2002; Rousseaux et al., 2004; Wierschem et al., 2008), the flumes were neither large enough nor counter-rotating to reduce rotating-frame effects and suppress secondary flows (Krishnappan, 1993; Petersen & Krishnappan, 1994; Z. Yang et al., 2000; S. Yang

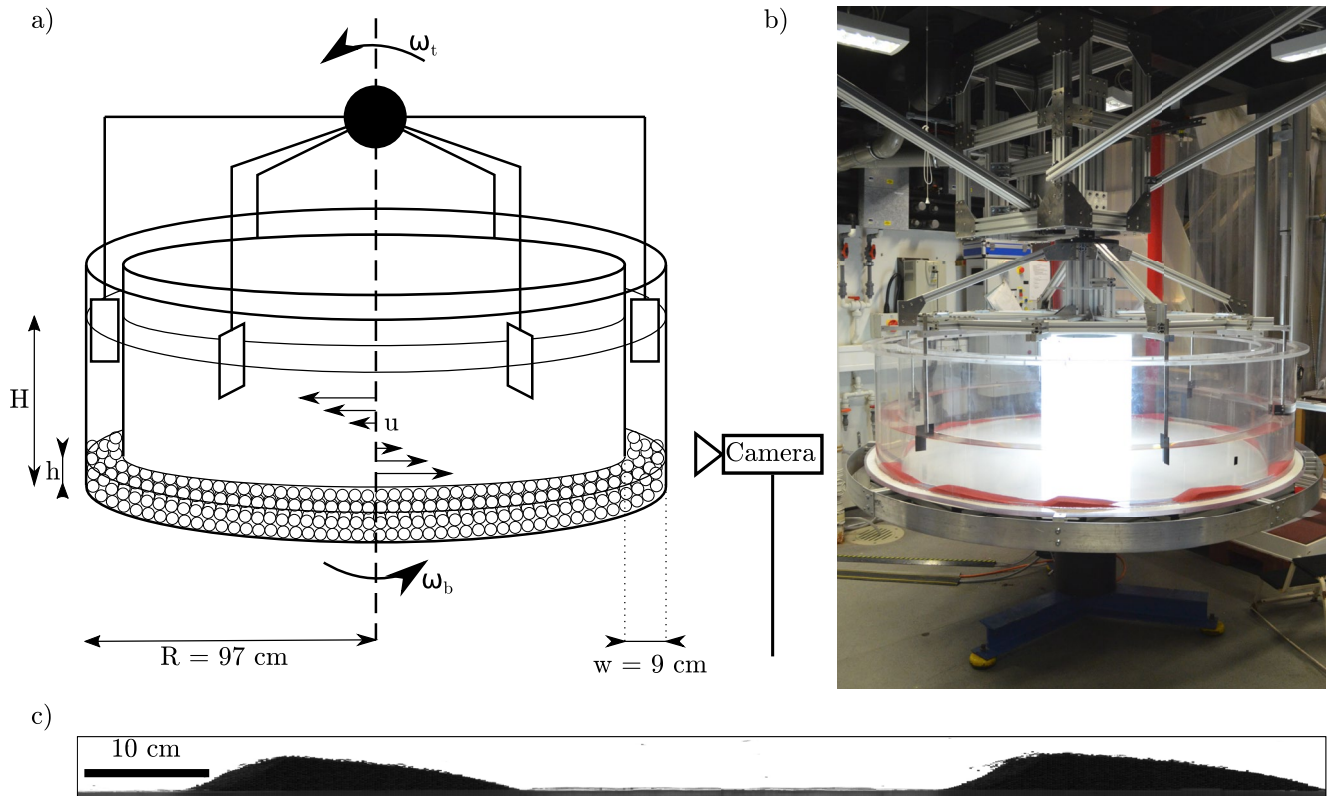


**Figure 1.** (a) Sketch and (b) photo of the experimental setup. The flume rotates at angular velocity  $\omega_b$ , whereas the paddles counter-rotate at  $\omega_t$ , creating a velocity profile  $u(z)$ . A fixed camera records a narrow section of the bed profile (100 px,  $\sim 1$  cm) at a frame rate of 200 Hz. The sediment bed height in each image is extracted. (c) Horizontal stack of 500 pixel columns, each from a consecutive image.

et al., 2015; Baar et al., 2018). In this study, we use a larger, counter-rotating set-up, previously presented by Bacik et al. (2020) and Bacik et al. (2021), to minimize secondary flows and investigate near-2D bedform formation and coarsening in a closed system over long periods.

### 3. Methods

#### 3.1. Experimental Set-Up

Experiments are performed in a counter-rotating annular channel of outer radius  $R = 97$  cm, height  $H = 50$  cm and width  $w = 9$  cm (Figure 1). The channel sits on a rotating table with a cylindrical LED array in the center allowing back lighting. A rotating assembly of six paddles with adjustable height fits into the top of the channel, providing a shearing top boundary condition. The channel is filled with water and monodisperse glass spheres (mean diameter  $d = 1.21$  mm, standard deviation  $\sigma = 0.08$  mm, measured with dynamic image analysis using a Bettersizer S3 Plus) of density  $\rho_p = 2.50 \pm 0.01$  g cm $^{-3}$  (determined from helium pycnometry using an Ultrapyc 1200e). The initial flat bed is created by lowering one paddle to the expected height of the bed surface and rotating the table slowly whilst making fine adjustments until we produce a constant bed thickness to within 3–4  $d$ . The paddles are then raised until their submerged depth is 6.4 cm.

The initial conditions are the sediment layer thickness  $h$ , water depth  $H$  and relative velocity between the flume and paddles  $U = R(\omega_t - \omega_b)$ , where  $\omega_t$  and  $\omega_b$  are the angular velocities of the paddles and table, respectively. Table S1 (Supporting Information S1) lists all the experimental conditions, but we select our parameters from  $h = 0.8, 1.6, \text{ or } 3.2$  cm,  $H = 20, 30, \text{ or } 40$  cm and vary  $U$  discretely from 0.61 to 1.52 m s $^{-1}$ . The table and paddles are accelerated to their target angular velocities within  $\sim 10$  s, creating a shear flow which, if fast enough ( $u_*$  greater than some threshold  $u_{*t}$ , corresponding to  $\theta_t$ ), lifts and displaces the particles. Particles are mobilized in all experiments ( $u_* > u_{*t}$ ) and the flow is turbulent (Reynolds number  $Re = Uw/\nu \gtrsim O(10^5)$ , where  $\nu = 10^{-6}$  m $^2$  s $^{-1}$

is the kinematic viscosity of water). Each experiment lasts 20 min. For each experiment, we estimate the transport stage (Bradley & Venditti, 2019)  $T = u_* / u_s$ , where  $u_s$  is the settling velocity of particles given by

$$u_s = \left( \frac{4gd(\rho_p - \rho_f)}{3\rho_f C_d} \right)^{1/2}, \quad (4)$$

and  $C_d$  is the drag coefficient which depends on the particle Reynolds number  $Re_p = u_* d / \nu$ , with different empirical parameterizations for  $C_d(Re_p)$  for different ranges of  $Re_p$ . In all cases,  $Re_p$  is between 90 and 230 and the corresponding relationship is  $C_d = 10 Re^{-1/2}$  (Bonadonna & Phillips, 2003; Kunii & Levenspeil, 1968). We are thus able to calculate values of  $u_s$  and  $T$  for all experiments (values in Table S1). For all experiments,  $3 \leq T \leq 5$ , demonstrating that these experiments are limited to the threshold transport stage (Bradley & Venditti, 2019).

Transverse variations in bedform morphology (Baar et al., 2018) are minimized by selecting the optimal value of  $r^* = |\omega_r / \omega_b|$  for each set  $\{h, H, U\}$ . As a result, we are able to produce almost two-dimensional dunes in our narrow channel without lateral variations. However, some three-dimensionality can be seen at dune crests, which are slightly pointed, and at the upstream feet of discrete dunes which have pointed contacts with the unerodible base. These variations, which are of the order of a few particle diameters and are due to a smaller flow velocity at the side-walls than the channel centerline, do not significantly impact our results.

Data is captured using an ISVI IC-X12CXP camera in a fixed position viewing the flume along a radial axis (Figure 1a). Images of  $(100 \times 2,048)$  px<sup>2</sup> are captured with a rate  $f = 200$  Hz and a spatial resolution of  $\sim 0.1$  mm px<sup>-1</sup>. Against the illuminated central column, the contrast in light intensity from the fluid and the sediment layers allows accurate measurement of the bed height to within  $0.8 d$ . As the table rotates, consecutive images are stitched together reproducing the bed profile (Figure 1c). The distance between the profile height measurements  $\Delta x = R\omega_b / f$  therefore ranges from 1.5 to 3.5 mm (Table S1, Supporting Information S1). These measurements enable quantification of the time evolution of the bed amplitude and number of peaks in the bed profile.

We also perform three separate particle-tracking velocimetry (PTV) experiments to visualize the flow profile inside the flume. In these experiments there is no sediment, that is,  $h = 0$  (to avoid dune formation),  $U = 1.02$  m s<sup>-1</sup> and  $H = 20, 30$ , or 40 cm. Neutrally buoyant, VTAC pliolite particles were suspended in the water and the flume was imaged with a fixed-position Photron camera at a frame rate of  $f = 1500$  Hz. The azimuthal velocity field is obtained through a PTV algorithm (Dalziel, 1992) and is then horizontally averaged to obtain the mean vertical velocity profile.

### 3.2. OpenFOAM Simulations

Whilst PTV measurements provide information on the flow profile, we are unable to resolve the near-wall ( $z < 1$  cm) velocity profile due to lack of near-wall resolution. Therefore, in order to constrain  $u_*$ , we perform Large Eddy Simulations (LES) of the fluid flow in the experiments, prior to the formation of dunes, using the open-access software OpenFOAM (Weller & Tabor, 1998). We model a simplified domain, consisting of a linear flume of the same width as in the experiment. The domain is periodic along its length, which is equal to  $1/6$  of the tank circumference. The side and basal walls have non-slip boundary conditions, whilst the base has a roughness height of 1.21 mm (equal to  $d$ ) and roughness constant 0.5. A free-slip boundary condition represents the air-water interface at the top of the domain. Deformation on the top and basal boundaries is neglected. In the middle of the length of the domain, a solid paddle of thickness 4 mm extends 6.4 cm (equal to the submerged length of the paddles in the experiment) from the upper surface into the domain interior. These solid surfaces have nonslip boundary conditions. In order to link the experiments and the simulations, the side and basal walls move with a horizontal velocity  $U$ , while the domain height is  $(H - h)$ . By varying both these quantities, we can span the experimental conditions used in the laboratory. Further details on the LES can be found in Supporting Information S1. We also perform additional simulations to reproduce the PTV experiments without sediment to validate the use of the LES. It is important to note that the value of  $u_*$  obtained through the LES only pertains to the initial stage of the experiment, as the formation of dunes will lead to temporal and spatial variations in basal shear stress (Lefebvre et al., 2013). However, since we ultimately relate  $u_*$  to the initial dune growth rate, this is acceptable for our purposes.

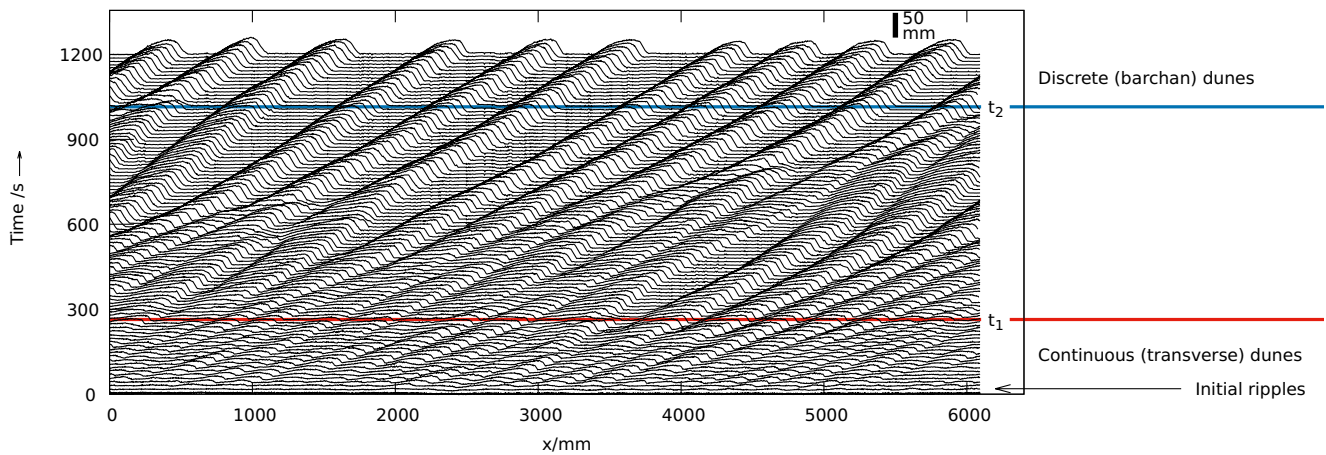


**Figure 2.** The bed profile  $Z(x, t)$  over 20 min for  $H = 20$  cm,  $h = 0.8$  cm, and  $U = 1.05$  m  $s^{-1}$ . Small perturbations form within 60 s before the profile coarsens through bedform interactions. After  $\sim 300$  s, flat sections in  $Z(x)$  appear where the channel base has been exposed ( $t_1$ , red line). Multiple patches of bare ground appear as the profile transitions from continuous to discrete dunes ( $t_2$ , blue line). The solid black bar indicates the vertical scale.

## 4. Results

### 4.1. Profile Evolution and Bedform Interactions

In order to quantify bedform development, successive profiles captured during the experiment are stacked together to produce space-time diagrams (e.g., Figure 2). Over time (the  $y$  axis), the bedform profile around the circumference (the  $x$  axis) transitions from a flat bed to small ripples, before coarsening to transverse and then discrete dunes. Initially, small-amplitude perturbations with irregular wavelength appear within  $\sim 60$  s. These perturbations grow and the peak-to-peak separation increases. Eventually, the first gap appears at  $t_1$  (red line) when the bed has eroded to the flume base for the first time, and  $t_2$  (blue line) represents the time when the last gap between dunes appears and no neighboring dunes are touching. Specifically, for the example in Figure 2,  $t_1 \approx 300$  s when the first gap appears at  $x \approx 3,500$  mm, and  $t_2 \approx 900$  s. Physically, this signifies a gradual transition from continuous bedforms ( $t < t_1$ ) to isolated dunes ( $t > t_2$ ), where the exact values of  $t_1$  and  $t_2$  depend on the values of  $H$ ,  $h$  and  $U$  (Figure S1 in Supporting Information S1). The discrete dunes are a 2D equivalent of 3D barchans, although the confined geometry prevents the formation of the distinctive horns. We also calculate the Fourier transform of each profile  $\tilde{z}(k)$ , where  $k$  is the wavenumber (Figure S2 in Supporting Information S1). However, we find that the modal wavenumber evolution in the spectrum is very noisy, whilst other characteristic quantities, such as the mean or higher order moments, depend on the spatial resolution of the bed profile down to the smallest scale we measure. We therefore choose not to use this data any further.

Coarsening throughout the experiment is controlled by coalescence and ejection interactions between neighboring bedforms, as has been previously observed (Baas, 1994; Coleman & Melville, 1994; Gao et al., 2015; Martin & Jerolmack, 2013). Figures 3a and 3c show an observed coalescence event, where a smaller and faster upstream dune collides with a larger, slower downstream dune. During coalescence, (a) the peaks approach each other, (b) the trough between them disappears, and (c) they merge into one bedform. Although during ejection (Figures 3b and 3d), the initial interaction seems similar to coalescence, the features are distinctly different. Initially, (1) mass is transferred to the upstream dune which grows whilst the downstream dune shrinks. Then, (2) the downstream and upstream dunes accelerate and decelerate, respectively, resulting in (3) the downstream peak being ejected from the intermediate structure. We observe that the two peaks never crossover, which is why we prefer not to refer to these interactions as “passing through” (Martin & Jerolmack, 2013). Since dunes in the experiment are often interacting with both upstream and downstream neighbors, dune-pair interactions rarely happen in isolation, for example, the upstream (blue) dune in Figure 3d maintains an almost constant velocity whilst undergoing ejection with a downstream neighbor, since it is affected by yet a further upstream neighbor. Both coalescence and ejection impact the coarsening of the bed profile; coalescence reduces the number of peaks  $n$  in the profile but increases the dune amplitude, whilst ejection conserves  $n$  but redistributes mass. We also note that, in addition to dune migration, some sediment transport occurs through a small number of particles in saltation or suspension,

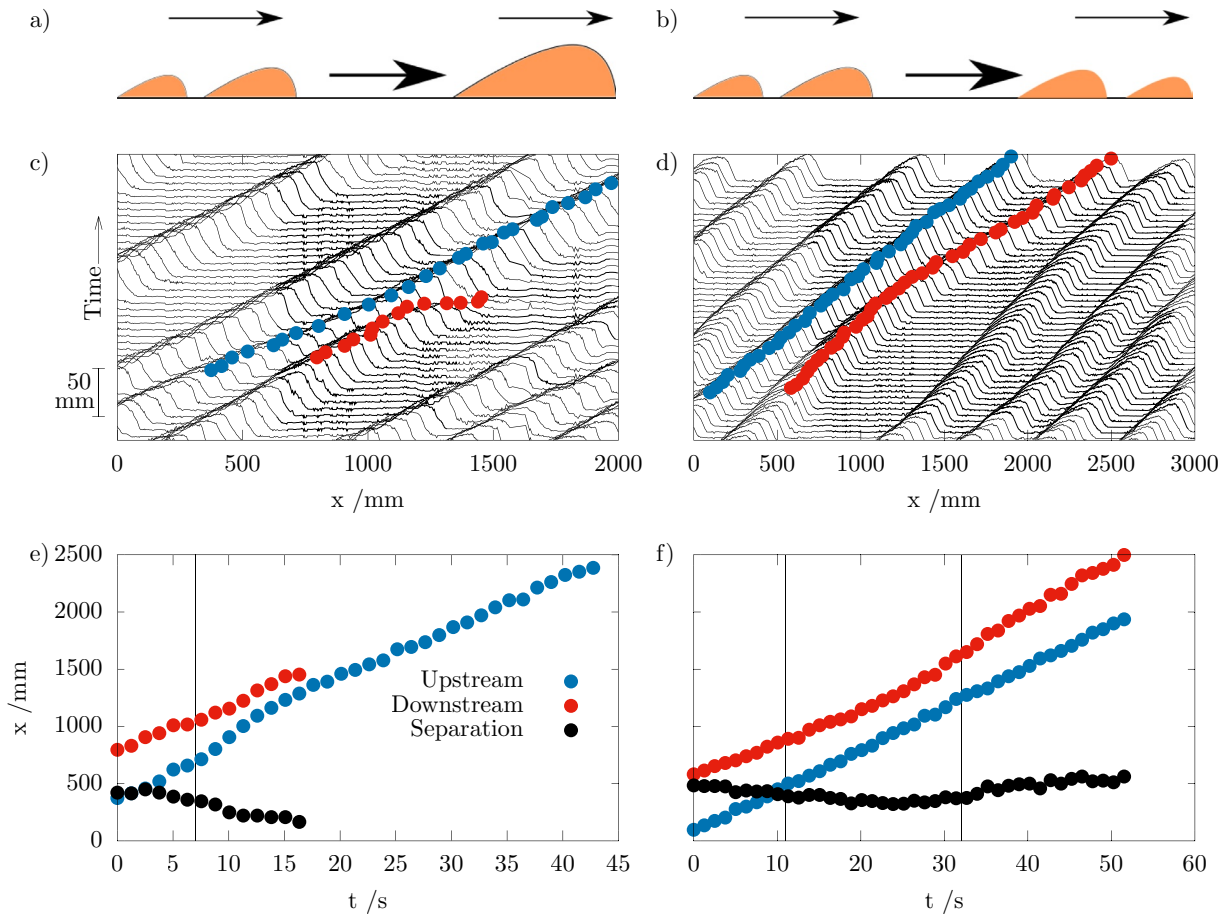


**Figure 3.** Comparison between coalescence and ejection. (a, c, e) A coalescence interaction ( $h = 0.8$  cm,  $H = 40$  cm,  $U = 1.32$  m s<sup>-1</sup>). The separation is the horizontal distance between peaks. The downstream dune is caught by the faster upstream dune and disappears into the upstream dune's slipface. The vertical line shows when the dunes first touched. (b, d, f) Ejection example ( $h = 0.8$  cm,  $H = 30$  cm,  $U = 1.22$  m s<sup>-1</sup>) where mass is transferred from the downstream to the upstream dune. The downstream dune shrinks and accelerates away. The upstream dune in this case keeps a relatively constant velocity since it has also just been ejected from another immediately upstream dune. The vertical lines in (e) and (f) show the moments when the dunes first make and break contact, which are definable in this case since the experiments have reached the discrete stage.

including particles which bypass dunes. The number of particles transported in such a way increases with flow rate, but always remains small and does not seem to have a significant impact on the coarsening behavior.

As a continuum description of coarsening, we define the root-mean-squared amplitude  $\bar{z}$  of the profile as

$$\bar{z} = \sqrt{\frac{1}{L} \int_0^L (Z(x) - \langle Z \rangle)^2 dx}, \quad (5)$$

where  $L = 2\pi R = 6.095$  m is the flume circumference,  $x$  the position coordinate,  $Z(x)$  the bed profile and  $\langle Z \rangle$  the mean bed height. We choose to use this measure since the peak-to-peak amplitude  $z_{\max}$  is sensitive to unusually large peaks and noisy due to fluctuations in the location of individual particles at bedform crests (Figure S3 in Supporting Information S1). Figure 4 shows  $\bar{z}$  as a function of time  $t$  for selected values of  $U$ ,  $H$ , and  $h$ . We avoid overcrowding the figure by only showing some experiments that show typical behavior and only consider experiments where bedform development was observed (Figure S4 in the Supporting Information S1 shows the equivalent curves for all experiments). Two distinct stages can be observed: (a) an initial growth of  $\bar{z}$  with  $t$  followed by, for some experiments, (b) saturation of  $\bar{z}$ . The transition time between the two stages depends on  $U$ ,  $H$  and  $h$ . This behavior appears similar, at least qualitatively, to that predicted by the exponentially saturated growth law (Equation 2).

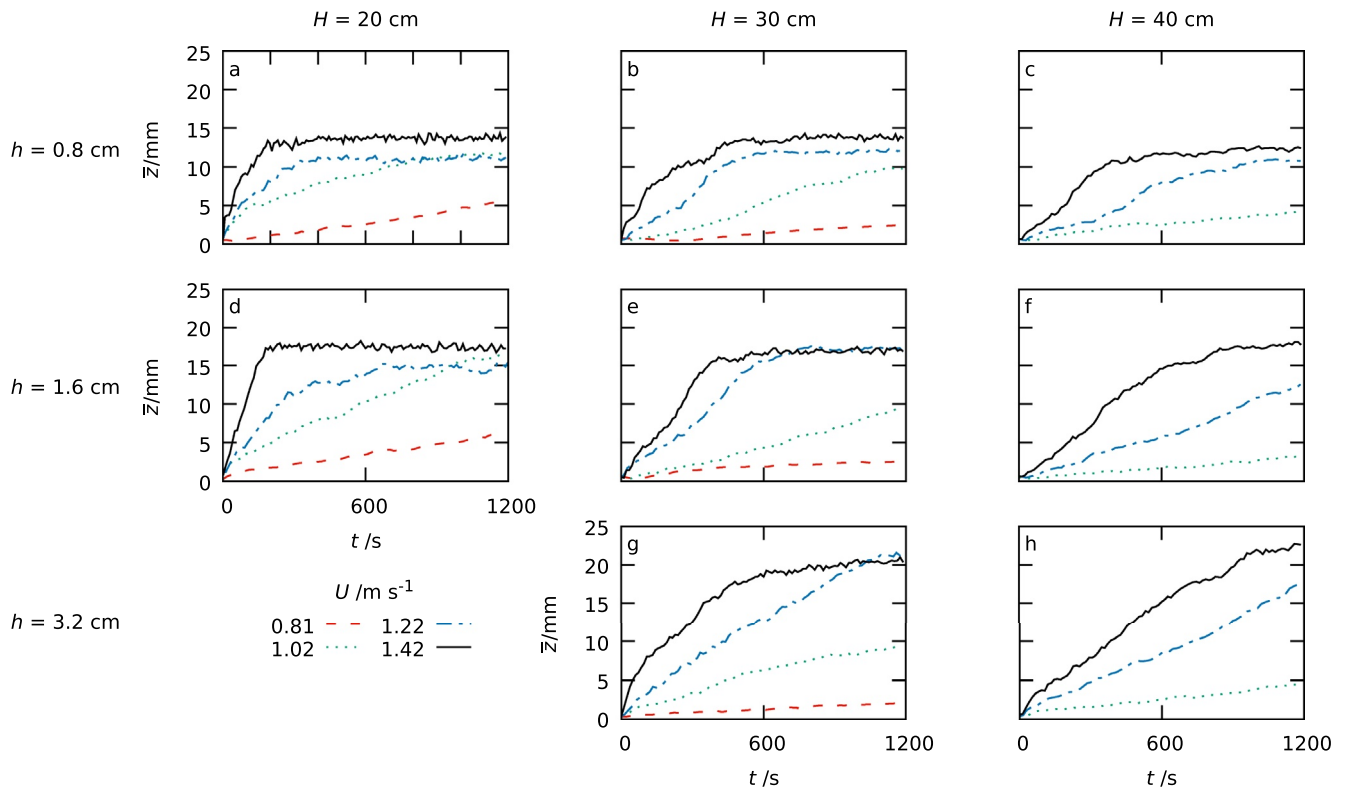


**Figure 4.** Root-mean squared amplitude  $\bar{z}$  of the bed as a function of time  $t$  for selected flow velocities  $U$ , initial bed thicknesses  $h$ , and flow depths  $H$ . All profiles show an increase in  $\bar{z}$  with  $t$ . In all experiments,  $\bar{z}$  appears to grow linearly, with the growth rate increasing with  $U$  before some experiments, with sufficiently large  $U$ , saturate. The saturation value is seemingly independent of  $H$  and  $U$  but increases with  $h$ .

In addition to  $\bar{z}$ , we also calculate the wavelength evolution during the experiment. As described above, the spectral properties of the bed profile depend on the spatial resolution of the data. We therefore choose to define the wavelength as

$$\lambda = L/n, \quad (6)$$

where  $n$  is the number of dunes in the flume and  $L$  is the flume circumference. We calculate  $n$  using a peak-finding algorithm following Martin and Jerolmack (2013) which ensures we capture as many small peaks as possible whilst not over-counting spurious peaks (Supporting Information S1). Figure 5 shows  $\lambda(t)$  for selected experiments. For  $H = 30$  cm,  $U = 0.81$  m s<sup>-1</sup>,  $\lambda$  only increases slightly during the experiment. These experiments showed little growth and the bed amplitude is sufficiently small that the peak-finding algorithm is inaccurate. In all other experiments,  $\lambda$  initially increases rapidly with  $t$  before plateauing. As with  $\bar{z}$ , it appears, at least qualitatively, that  $\lambda$  exhibits exponentially saturated growth, an observation which we go on to quantify in Section 4.3.

Whilst these observations of  $\bar{z}(t)$  and  $\lambda(t)$  provide descriptive information on how coarsening proceeds, understanding of the underlying dynamics requires us to link these quantities to the driving fluid flow. We therefore now present results of LES which relate  $\{U, H, h\}$  to  $u_*$ .

#### 4.2. Flow Profiles and Basal Shear Stress

In order to quantitatively relate dune formation and evolution to the driving fluid flow, we first need to relate the experimental conditions, defined by  $\{U, H, h\}$ , to  $u_*$ . We achieve this through LES, using techniques described in Section 3.2. To be confident that LES can capture the fluid flow in the flume, we compare modeled width-averaged and center-line horizontal flow profiles, in the absence of sediment, with experimental PTV measurements (Figure 6) for  $U = 1.02$  m s<sup>-1</sup> and  $H = 20, 30,$  and  $40$  cm. We observe that the PTV data qualitatively agrees very well with the simulated center-line velocity profile, suggesting more particles are sampled in the center of the



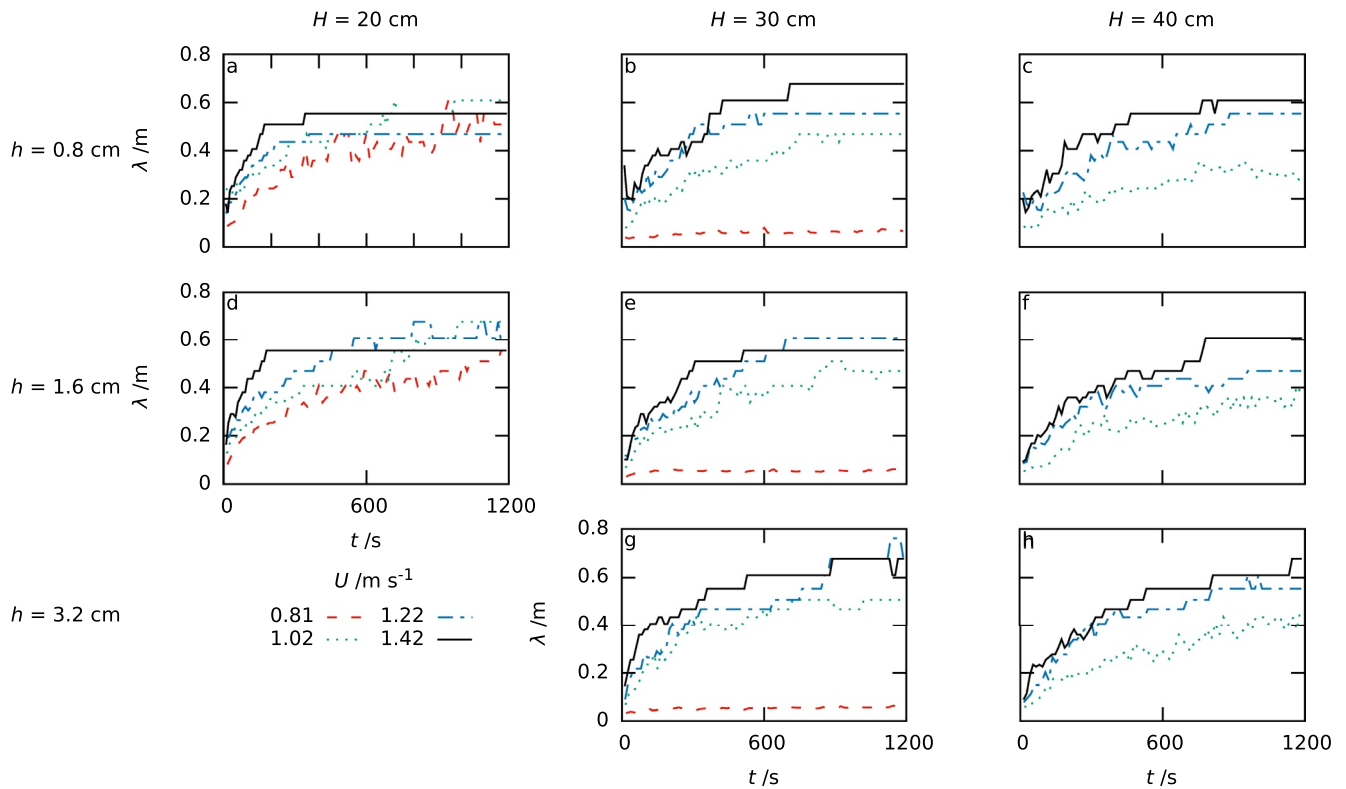


**Figure 5.** Evolution of the wavelength  $\lambda$  of the bed profile for selected flow velocities  $U$ , bed thicknesses  $h$  and flow depths  $H$ . For  $H = 30$  cm and  $U = 0.81$  m s<sup>-1</sup>,  $\lambda$  only slightly increases during the experiment and, since these experiments show limited growth (Figure 4), the peak-detection algorithm does not work well. Hence,  $\lambda$  only slightly increased and absolute values should be treated cautiously. All other experiments show apparent exponentially saturated growth, similar to the bed amplitude seen in Figure 4.

flume and therefore the experimental average is reliable. However, in the near-boundary region for  $z < 5$  cm, the PTV data fails to reproduce the simulated velocities. The low-resolution of the PTV and interactions between tracer particles and the flume base prevent accurate measurement of the expected large velocity gradient in this region. Therefore, we use the LES to constrain the basal shear stress.

Motivated by the strong agreement between the simulated and measured flow profiles, we now determine width-averaged velocity profiles for different values of  $H$ ,  $h$  and  $U$  that span the experimentally investigated

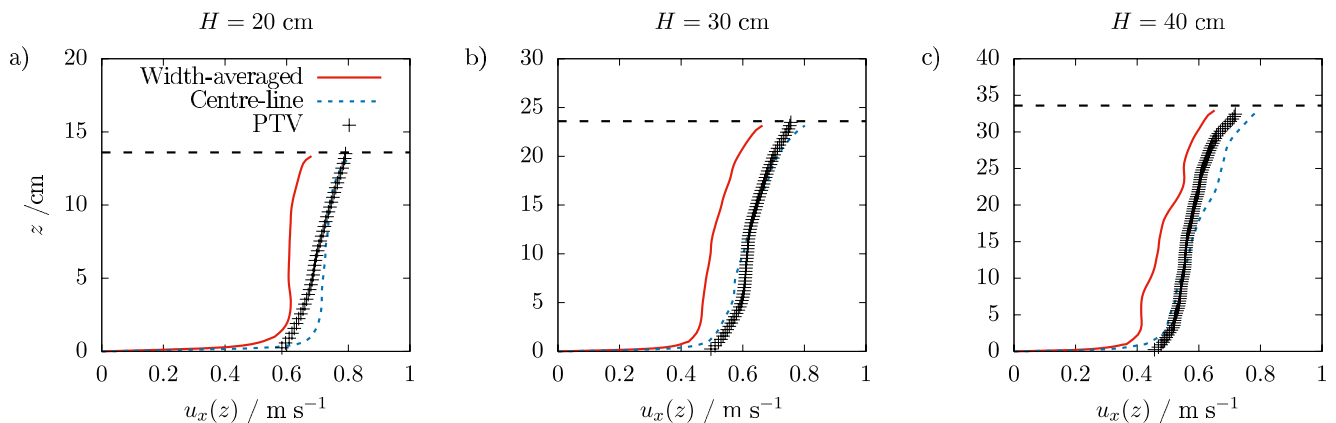


**Figure 6.** Simulated width-averaged and center-line velocity profiles and particle-tracking velocimetry (PTV) data for when the flume contains no sediment ( $h = 0$ ) and  $U = 1.02$  m s<sup>-1</sup> for (a)  $H = 20$ , (b) 30, and (c) 40 cm. Horizontal dashed lines show the height of the bottom of the paddles. The frame of reference is taken such that the base and side walls of the flume are stationary.

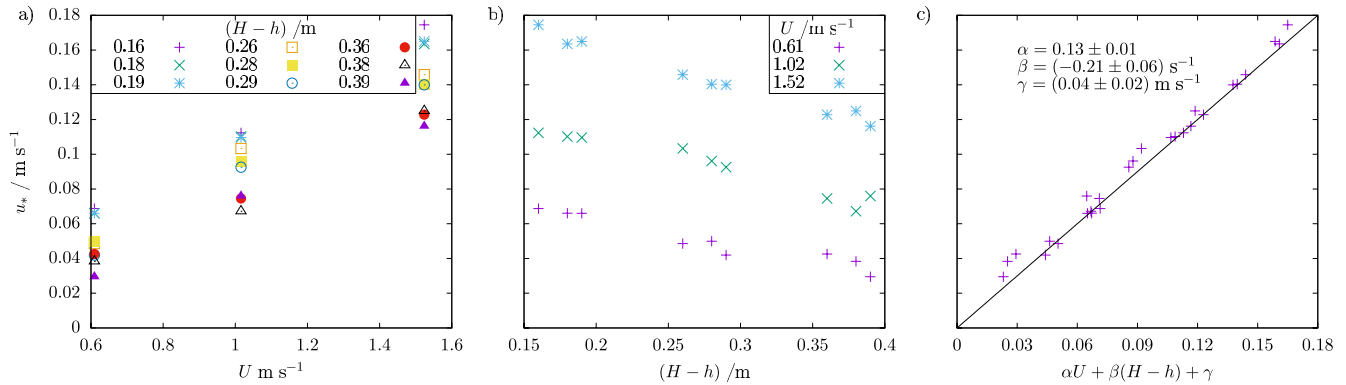


**Figure 7.** Simulated values of  $u_*$  for selected experimental conditions, as a function of (a)  $U$  and (b)  $H - h$ . (c)  $u_*$  plotted against the planar fit (Equation 8), compared to the 1:1 line.

parameter space (Figure S5 in Supporting Information S1). All of the flow profiles have a similar shape with the velocity rapidly increasing with height for  $z < 1$  cm, then maintaining an almost constant velocity in the bulk of the flow, before increasing again near the top. The lowermost 0.5 cm of the profile appears to be log-linear so we constrain the basal shear stress at the start of each experiment by fitting to this segment the log-law of the wall (von Kármán, 1930; Thompson et al., 2004)

$$u_x(z) = \frac{u_*}{\kappa} \ln \frac{z}{z_0}, \quad (7)$$

where  $\kappa = 0.41$  is the von Kármán constant and  $z_0$  the roughness length. Figures 7a and 7b show the calculated values of  $u_*$  as a function of  $U$  and  $(H - h)$ .  $u_*$  depends approximately linearly on both  $U$  and  $H - h$  in the portion of the parameter space we experimentally sample. We therefore fit the data to the empirical relationship

$$u_* = \alpha U + \beta(H - h) + \gamma, \quad (8)$$

and find fitted values of  $\alpha = 0.13 \pm 0.01$ ,  $\beta = (-0.21 \pm 0.06) \text{ s}^{-1}$ , and  $\gamma = (0.04 \pm 0.02) \text{ m s}^{-1}$  and a coefficient of determination  $R^2 = 0.95$ . Figure 7c shows the simulated values of  $u_*$  plotted against the value predicted by the fit; since the points plot very close to the 1:1 line the fit is considered reliable for this portion of the parameter space.

### 4.3. Connecting Dune Growth Rate and Friction Velocity

For each experiment, we fit  $\bar{z}(t)$  (Figure 4) and  $\lambda(t)$  (Figure 5) to the exponentially saturating growth laws (Equations 2 and 3, respectively) to model the saturation amplitude and wavelength as well as the associated growth rates. The fitted values of  $a_z$ ,  $b_z$ ,  $a_\lambda$ , and  $b_\lambda$  can be found in Table S1. These quantities provide information on the coarsening dynamics. First,  $a_z$  and  $a_\lambda$  can clearly be identified as the saturation amplitude and wavelength of the dune pattern. Furthermore, the initial growth rate of the  $\bar{z}$  and  $\lambda$  can be obtained by differentiating Equations 2 and 3 to obtain

$$\dot{\bar{z}} = a_z b_z e^{-b_z t} \approx a_z b_z, \quad \text{for } b_z t \ll 1, \quad (9)$$

and

$$\dot{\lambda} = a_\lambda b_\lambda e^{-b_\lambda t} \approx a_\lambda b_\lambda, \quad \text{for } b_\lambda t \ll 1, \quad (10)$$

respectively, where the final approximation is obtained by taking the first term of the Taylor expansion of the exponential and is only valid at early times. Finally, we can use the fitted values of  $b_z$  and  $b_\lambda$  as an indication of experiments which attain saturation during the 20 min duration. If, for  $t = 1,200$  s,  $b_z t$  and/or  $b_\lambda t \geq 3$ , then we define that the amplitude and/or wavelength has saturated.

We find that only 22 out of our 61 experiments reach amplitude saturation (Table S1, Supporting Information S1). For these experiments, Figure 8a shows fitted values of  $a_z$ , the saturation amplitude, to be controlled only by the sediment height  $h$  and not the flow depth  $H$ . Fitted values of  $a_z$  for amplitude-unsaturated experiments are

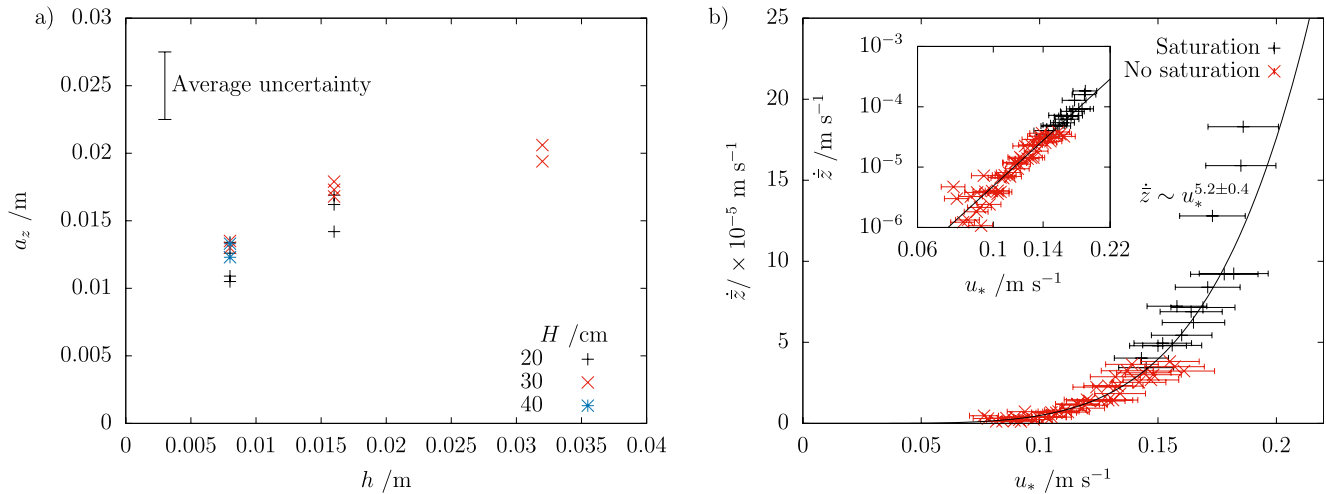


**Figure 8.** (a) Fitted value of  $a_z$  as a function of  $h$  for experiments where amplitude saturation is attained. (b) Initial growth rate  $\dot{z} = a_z b_z$  as a function of  $u_*$ . Experiments where amplitude saturation was reached are in black whilst those where the bedform amplitude was still growing at the end of the experiment are in red. The black line represents the fitted power law  $\dot{z} \sim u_*^{5.2 \pm 0.4}$ . Inset: Same but with logarithmic axes.

poorly constrained and therefore not shown here. We also plot the fitted initial growth rate  $\dot{z} = a_z b_z$  as a function of  $u_*$  (Figure 8b), where the latter is determined from Equation 8, for each experiment. We see that for all experiments, regardless of whether or not amplitude saturation is attained,  $\dot{z}$  strongly increases with  $u_*$ . In fact, fitting a power-law relationship, we find  $\dot{z} \sim u_*^{5.2 \pm 0.4}$ .

An alternative means of calculating the growth rate would be to fit a straight line to the initial part of the  $\bar{z}(t)$  curves and determine the gradient  $\dot{z}_{\text{lin}}$ . However, the limited temporal resolution of our data means there is often very few points (sometimes no more than three) in this region. Nonetheless, in Figure S6a in Supporting Information S1, we plot  $\dot{z}_{\text{lin}}$  against  $\dot{z} = a_z b_z$  and find that the obtained values are broadly comparable. Furthermore, we fit a power-law relationship between  $\dot{z}_{\text{lin}}$  and  $u_*$  and find  $\dot{z}_{\text{lin}} \sim u_*^{4.8 \pm 0.5}$  (Figure S6b in Supporting Information S1). The exponent here is slightly lower than that found when determining the growth rate with the exponentially saturated fitting, although they are within uncertainty.

It should be noted that our observed exponentially saturating growth contrasts with that observed in cellular automaton simulations of bedform coarsening (Gao et al., 2015) which exhibited power-law growth  $\bar{z} \sim t^{1/3}$ . However, our experiments consider a sediment-limited regime, with the unerodible base exposed during coarsening, whilst Gao et al. (2015) simulated bedforms on an infinitely thick bed. Another difference is that the flow in our experiments is driven by paddles, giving rise to turbulent fluctuations which may also play a role. Figure S7 in Supporting Information S1, presents a comparison of our results to the scaling of Gao et al. (2015).

At very early times, the growth is sometimes slower than that predicted by Equation 9, for example,  $U = 0.81 \text{ m s}^{-1}$ ,  $h = 0.8 \text{ cm}$ ,  $H = 30 \text{ cm}$  (Figure 4b), where  $\bar{z}$  initially decreases before increasing, suggesting a stage of bed compaction prior to bedform growth. At late times, saturation only occurs once only discrete dunes are present. For further growth to occur, coalescence-type interactions must happen. However, at this stage interactions occur infrequently (Figure 2) since the dunes all migrate at a similar speed, and are almost all collisions of ejection-type. Therefore, further growth is only achieved through occasional coalescence events that appear as step-like jumps in the  $\bar{z}(t)$  profiles (e.g., Figure 4b,  $U = 1.42 \text{ m s}^{-1}$  at  $t \approx 300 \text{ s}$ ). Some longer duration experiments have been performed and we observe that once the discrete stage has been reached, dune collisions almost entirely cease and no further coarsening occurs.

In contrast to the amplitude saturation results, all but four of the experiments attained wavelength-saturation prior to the end of the experiment. Furthermore, while Figure 8 shows strong systematic dependencies of  $a_z$  and  $\dot{z} = a_z b_z$  on the initial flow conditions  $h$  and  $u_*$ , respectively, we do not observe the same for  $a_x$  and  $b_x$ . However, some correlations can be identified although the data are widely scattered preventing significant empirical relationships from being determined. In contrast to  $a_z$ , we find that  $a_x$  correlates most strongly with  $u_*$  rather than  $h$ , with  $a_x$  increasing with  $u_*$ . This is shown in Figure 9a, where the different symbols correspond to different values

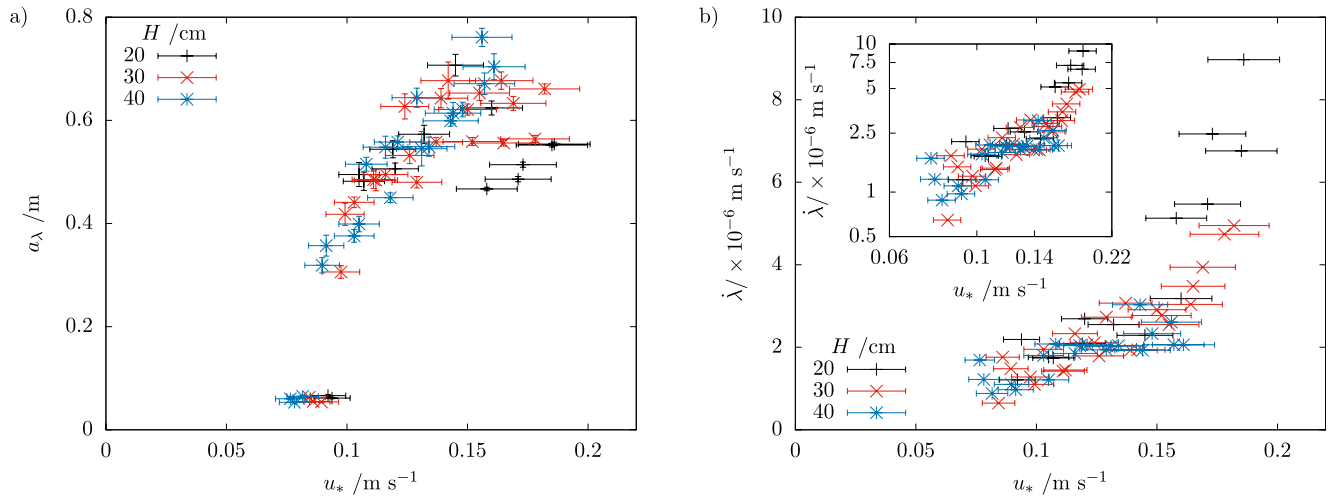


**Figure 9.** (a) Fitted value of  $a_\lambda$  as a function of  $u_*$  for different values of  $H$ . Initial growth rate of the wavelength  $\dot{\lambda}$  as a function of  $u_*$ . Inset: same but with logarithmic axes.

of  $H$ . It can be seen that although  $a_\lambda$  generally increases with  $u_*$ , there is significant scatter. This is particularly evident for high  $u_*$ , where values of  $a_\lambda$  for  $H = 20$  or  $30$  cm appear significantly lower than most of the data. Figure 9b shows  $\dot{\lambda} = a_\lambda b_\lambda$ , which is representative of the initial growth rate of  $\lambda$  as a function of  $u_*$ . As with  $\dot{z}$ , there is positive correlation between the two. However, it is not possible to fit the data with a single power law. For  $u_* \lesssim 0.18$ ,  $a_\lambda b_\lambda$  increases with  $u_*$  but the data is widely scattered while, for  $u_* \gtrsim 0.18$ , there is still an increasing trend but the rate of increase appears significantly higher.

## 5. Discussion

Our results have shown that the amplitude and wavelength evolution of dunes in a narrow channel can be well-modeled with exponentially saturated growth laws (Equations 2 and 3, respectively). Although some studies have reported power-law growth (Coleman et al., 2005; Gao et al., 2015; Nikora & Hicks, 1997), our observations are consistent with many other experimental and numerical observations (Baas, 1994; Bradley & Venditti, 2019; Swanson et al., 2017; Venditti et al., 2005a). A key difference of our studies compared to previous work is that we have investigated the growth of dunes from a thin layer of sediment, rather than a bed thick enough that an unerodible base is never exposed. Thus, the growth of bedforms in our experiment is limited by sediment availability, rather than the water depth or the flow speed. This is demonstrated by the fact that the saturation amplitude  $a_z$  increases with the initial sediment layer thickness  $h$  (Figure 8a). As such, this work has most relevance to rivers with limited sediment supply (Carling et al., 2000; Kleinhans et al., 2002; Mantz, 1978; McCulloch & Janda, 1964; Tuijinder et al., 2009).

We further show that the initial growth rate of the amplitude of the dunes, given by the product  $\dot{z} = a_z b_z$  of the fitted parameters in Equation 2, strongly depends on the friction velocity  $u_*$  (Figure 8). Specifically, we find a power law  $\dot{z} \sim u_*^{5.2 \pm 0.4}$ . This is despite the fact that our estimate of  $u_*$  is strictly only valid at the experimental onset, when the sediment layer is flat. Over time, feedback between the evolving sediment surface and the fluid flow will cause  $u_*$  to spatially and temporally vary (Lefebvre et al., 2013). Whilst this may explain some of the scatter in the data, since  $\dot{z} = a_z b_z$  is true for only very early times (i.e.,  $t \ll 1/b_z$ ), it can be assumed that surface topography does not significantly affect  $u_*$  during this stage. However, more detailed investigation of the fluid flow within the experiment, potentially through ultrasonic measurements (Hurther et al., 2011; Naqshband et al., 2014), could be used to better understand this.

Whilst the result  $\dot{z} \sim u_*^{5.2 \pm 0.4}$  is significant, we currently have no theoretical reasoning or model explaining this outcome. However, two features of the obtained power-law could motivate future work. First, it is worth noting that the fitted empirical law does not allow for a threshold friction velocity  $u_{*t}$ . Indeed, we find that when attempting to fit a function of the form  $\dot{z} \sim (u_* - u_{*t})^\epsilon$ , where  $\epsilon$  is the free parameter, the best quality fit, as determined by evaluation of an  $R^2$  value, is obtained for  $u_{*t} = 0$ . Our power-law is similar in form to some empirical laws

that have been proposed to relate sediment transport rates to the driving shear stress and also do not depend on a threshold (Lavelle & Mojfeld, 1987; Paintal, 1971). This suggests that, if any threshold exists, it perhaps needs to be defined in a statistical, rather than deterministic sense, since turbulent fluctuations can drive fluid motion even if the mean shear stress is insufficient (Pächtz et al., 2020).

Second, if we express the power-law in terms of the Shields number  $\Theta$ , rather than  $u_*$  (see Equation 1), we obtain  $\bar{z} \sim \Theta^{2.6 \pm 0.2}$ . The exponent here is similar to that obtained by Paintal (1971) for the relationship between the sediment transport rate  $Q$  and  $\theta$  who found, for  $\theta > \theta_t \approx 0.05$ ,  $Q \sim \theta^{2.5}$ . For our experimental conditions, the condition  $\theta_t = 0.05$  corresponds to  $u_{*,t} \approx 0.03$ , such that this threshold is below the range of  $u_*$  explored in our experiments (see Figure 8). This suggests that the initial dune growth rate in the coarsening regime may scale with the sediment transport rate. However, a plethora of parameterizations  $Q(u_*)$  exist (Lajeunesse et al., 2010; Meyer-Peter & Müller, 1948; Pächtz & Durán, 2020), meaning any given transport law must be used with care. Nonetheless, a proportionality between dune growth rate and  $Q$  is also predicted by linear stability analyses which predict the growth rate prior to coarsening (Colombini & Stocchino, 2008, 2011; Fourrière et al., 2010; Lü et al., 2021). Our results suggest that this dependence may also be valid in the coarsening regime.

Although we have been able to quantitatively relate the bedform amplitude evolution to the driving flow, this has not been the case for the wavelength evolution. In particular, while we see that both  $a_\lambda$  and  $\dot{\lambda} = a_\lambda b_\lambda$  positively correlate with  $u_*$ , the data is widely scattered. We also note that, throughout our experiments, the wavelength saturates prior to the amplitude, which is reflected in the fact that only four of our experiments do not reach wavelength saturation whereas 39 do not reach amplitude saturation. This is a consequence of deriving the wavelength from the number of peaks  $n$ . The number of peaks reaches an almost constant value once unerodible gaps have appeared in the sediment bed. Thus, even though bedforms in the discrete stage may change in length, this information is not recorded in our measure of wavelength. An alternative approach would perhaps be to measure the length of individual dunes rather than the wavelength. Whilst this would provide more insight into individual dune morphology, information on dune spacing would be lost, negatively impacting what could be inferred about coarsening of the overall dune pattern. A statistical measure of  $\lambda$  derived from spectral measurements (see Figure S2b in Supporting Information S1) could possibly capture the morphologies of both individual dunes and the overall pattern. However, we find such measures to depend on our spatial resolution, hence improved data collection methods are necessary to achieve this.

It is worth emphasising that our results concern growth during the coarsening stage of bedform growth. According to dune instability theory, this should be preceded by a linearly unstable regime where the bed amplitude grows exponentially (Andreotti et al., 2002b; Charru et al., 2013; Colombini & Stocchino, 2011; Fourrière et al., 2010; Gadal et al., 2018). At no point during our experiments do we observe such growth, an observation consistent with other aqueous flume experiments (Baas, 1994; Bradley & Venditti, 2017; Coleman & Melville, 1994). This suggests that the linear regime, if it exists, only persists for a timescale too short for us to observe. Measurements of extremely early dune growth represent a technical challenge, particularly for  $u_* \gg u_{*,t}$ , and experimental validation of dune instability theory in aqueous environments remains lacking.

In addition to further investigation of the early time behavior, future studies could also address coarsening of 3D dune fields. Although studies of 2D dunes are easier to achieve in the laboratory, the majority of naturally occurring dunes exhibit three-dimensionality (Allen, 1968). As well as enabling a greater range of dune collision outcomes (Assis & Franklin, 2020; Durán et al., 2005; Endo et al., 2004; Hersen, 2005), the presence of 3D topography also impacts the turbulent structures that form in the overlying flow (Hardy et al., 2021; Maddux et al., 2003; Venditti, 2007). In fact, it has been shown that flows over 3D dunes exhibit significantly more turbulent vortices than for their 2D counterparts (Hardy et al., 2021). Given that these vortices contribute to the spatial and temporal variations of the basal shear stress, and that turbulent structures have been shown to impact dune collisions and interactions (Bacik et al., 2020, 2021), it will be critical for three-dimensionality to be accounted for when modelling bedform coarsening in natural rivers.

## 6. Conclusions

We have experimentally observed bedform coarsening, from small disturbances on a flat bed through continuous transverse dunes to discrete dunes. We quantify the coarsening using the temporal dependence of the bed amplitude  $\bar{z}$  and number of peaks in the profile  $n$ . Additionally, we have complemented the experiments with LES

to relate the dune formation and coarsening dynamics to  $u_*$ . In the experiments, we observe that bedforms first nucleate as small, irregular perturbations which grow to form continuous and then discrete dunes. We find that the root-mean-squared amplitude of the bed profile increases with time and is well-fitted by an exponentially saturated growth law. Although this is consistent with previous experimental (Baas, 1994; Coleman & Melville, 1994; Venditti et al., 2005a) and field (Fourrière et al., 2010) observations, we further find that the growth rate  $\dot{z}$  depends on  $u_*$  according to an empirical power law  $\dot{z} \sim u_*^5$ . Whilst this successfully captures the very strong dependence of  $\dot{z}$  on  $u_*$ , a theoretical prediction for this result lacks at this moment in time. Thus, further work is required to understand the growth of subaqueous dunes during non-linear coarsening.

## Data Availability Statement

Experimental data can be found at <https://doi.org/10.17863/CAM.39273>.

## Acknowledgments

This research was funded by Royal Society Challenge Grant CH160065 and Isaac Newton Trust Early Career Grant RG 74916. N. M. Vriend was supported by a Dorothy Hodgkin Fellowship DH120121 and a Royal Society University Research Fellowship No. URF/R1/191332. K. A. Bacik acknowledges a PhD studentship from Schlumberger Cambridge Research Limited. The authors thank David Page-Croft, John Milton, Paul Mitton, Colin Hitch and Andrew Denson for their technical expertise and Stuart Dalziel for useful discussions. The authors also thank Suleyman Naqshband and four anonymous reviewers, as well as the editor A. J. F. Hoitink and the associate editor, for helpful and insightful comments on a previous version of this paper. C. N acknowledges support from the UnivEarthS LabEx program of Sorbonne Paris Cité (ANR-10-LABX-0023 and ANR-11-IDEX-0005-002) and the French National Research Agency (ANR-17-CE01-0014/SONO).

## References

- Allen, J. R. L. (1968). The nature and origin of bedform hierarchies. *Sedimentology*, *10*, 161–182. <https://doi.org/10.1111/j.1365-3091.1968.tb01110.x>
- Amos, C. L., Grant, J., Daborn, G. R., & Black, K. (1992). Sea carousel: A benthic, annular flume. *Estuarine, Coastal and Shelf Science*, *34*, 557–577. [https://doi.org/10.1016/s0272-7714\(05\)80062-9](https://doi.org/10.1016/s0272-7714(05)80062-9)
- Andreotti, B., Claudin, P., & Douady, S. (2002a). Selection of dune shapes and velocities part 1: Dynamics of sand, wind and barchans. *European Physical Journal B*, *28*, 321–339. <https://doi.org/10.1140/epjb/e2002-00236-4>
- Andreotti, B., Claudin, P., & Douady, S. (2002b). Selection of dune shapes and velocities part 2: A two-dimensional modelling. *European Physical Journal B*, *28*, 341–352. <https://doi.org/10.1140/epjb/e2002-00237-3>
- Assis, W. R., & Franklin, E. M. (2020). A comprehensive picture for binary interactions of subaqueous barchans. *Geophysical Research Letters*, *47*. <https://doi.org/10.1029/2020gl089464>
- Baar, A. W., de Smit, J., Uijttewaai, W. S. J., & Kleinhans, M. G. (2018). Sediment transport of fine sand to fine gravel on transverse bed slopes in rotating annular flume experiments. *Water Resources Research*, *54*, 19–45. <https://doi.org/10.1002/2017wr020604>
- Baas, J. H. (1994). A flume study on the development and equilibrium morphology of current ripples in very fine sand. *Sedimentology*, *41*, 185–209. <https://doi.org/10.1111/j.1365-3091.1994.tb01400.x>
- Baas, J. H. (1999). An empirical model for the development and equilibrium morphology of current ripples in fine sand. *Sedimentology*, *46*, 123–138. <https://doi.org/10.1046/j.1365-3091.1999.00206.x>
- Bacik, K. A., Caulfield, C. P., & Vriend, N. M. (2021). Stability of the interaction between two sand dunes in an idealized laboratory experiment. *Physical Review Letters*, *127*, 154501. <https://doi.org/10.1103/physrevlett.127.154501>
- Bacik, K. A., Lovett, S., Caulfield, C. P., & Vriend, N. M. (2020). Wake-induced long range repulsion of aqueous dunes. *Physical Review Letters*, *124*, 054501. <https://doi.org/10.1103/physrevlett.124.054501>
- Bagnold, R. A. (1941). *The physics of blown sand and desert dunes*. Dover Publications Inc.
- Barnard, P. L. (2006). Giant sand waves at the mouth of San Francisco Bay. *Eos*, *87*, 285–289. <https://doi.org/10.1029/2006eo290003>
- Best, J. (1995). The fluid dynamics of river dunes: A review and some future research directions. *Journal of Geophysical Research: Earth Surface*, *110*, 2156–2202.
- Betat, A., Frette, V., & Rehberg, I. (1999). Sand ripples induced by water shear flow in an annular channel. *Physical Review Letters*, *83*, 88–91. <https://doi.org/10.1103/physrevlett.83.88>
- Betat, A., Kruelle, C. A., Frette, V., & Rehberg, I. (2002). Long-time behaviour of sand ripples induced by water shear flow. *European Physical Journal E*, *8*, 465–476. <https://doi.org/10.1140/epjef/2001-10110-y>
- Bonadonna, C., & Phillips, J. C. (2003). Sedimentation from strong volcanic plumes. *Journal of Geophysical Research*, *B7*, 2340. <https://doi.org/10.1029/2002jb002034>
- Bradley, R. W., & Venditti, J. G. (2017). Reevaluating dune scaling relations. *Earth-Science Reviews*, *165*, 356–376. <https://doi.org/10.1016/j.earscirev.2016.11.004>
- Bradley, R. W., & Venditti, J. G. (2019). The growth of dunes in rivers. *Journal of Geophysical Research: Earth Surface*, *124*, 548–566. <https://doi.org/10.1029/2018jf004835>
- Buffington, J. M., & Montgomery, D. R. (1997). A systematic analysis of eight decades of incipient motion studies, with special reference to gravel-bedded rivers. *Water Resources Research*, *33*, 1993–2029. <https://doi.org/10.1029/96wr03190>
- Carling, P. A., Gölz, E., Orr, H. G., & Radecki-Pawlik, A. (2000). The morphodynamics of fluvial sand dunes in the River Rhine, near Mainz, Germany. I. Sedimentology and morphology. *Sedimentology*, *47*, 227–252. <https://doi.org/10.1046/j.1365-3091.2000.00290.x>
- Charru, F., Andreotti, B., & Claudin, P. (2013). Sand ripples and dunes. *Annual Review of Fluid Mechanics*, *45*, 469–493. <https://doi.org/10.1146/annurev-fluid-011212-140806>
- Charru, F., Mouilleron, H., & Eiff, O. (2004). Erosion and deposition of particles on a bed sheared by a viscous flow. *Journal of Fluid Mechanics*, *519*, 55–80. <https://doi.org/10.1017/s0022112004001028>
- Coleman, S. E., & Melville, B. W. (1994). Bed-form development. *Journal of Hydraulic Engineering*, *120*, 544–560. [https://doi.org/10.1061/\(asce\)0733-9429\(1994\)120:5\(544\)](https://doi.org/10.1061/(asce)0733-9429(1994)120:5(544))
- Coleman, S. E., Zhang, M. H., & Clunie, T. M. (2005). Sediment-wave development in subcritical water flow. *Journal of Hydraulic Engineering*, *131*, 39–57. [https://doi.org/10.1061/\(asce\)0733-9429\(2005\)131:2\(106\)](https://doi.org/10.1061/(asce)0733-9429(2005)131:2(106))
- Colombini, M., & Stocchino, A. (2008). Finite-amplitude river dunes. *Journal of Fluid Mechanics*, *611*, 283–306. <https://doi.org/10.1017/s0022112008002814>
- Colombini, M., & Stocchino, A. (2011). Ripple and dune formation in rivers. *Journal of Fluid Mechanics*, *673*, 121–131. <https://doi.org/10.1017/s0022112011000048>
- Csahók, Z., Misbah, C., Rioual, F., & Valance, A. (2000). Dynamics of aeolian sand ripples. *European Physical Journal E*, *3*, 71–86. <https://doi.org/10.1007/s101890070043>

- Dalziel, S. B. (1992). Decay of rotating turbulence: Some particle tracking experiments. *Applied Scientific Research*, 49, 217–244. <https://doi.org/10.1007/bf00384624>
- Dinega, S., Glasner, K., & Byrne, S. (2010). Long-time evolution of models of aeolian sand dune fields: Influence of dune formation and collision. *Geomorphology*, 121, 55–68. <https://doi.org/10.1016/j.geomorph.2009.02.010>
- Durán, O., Schwämmle, V., & Herrmann, H. (2005). Breeding and solitary wave behavior of dunes. *Physical Review E - Statistical Physics, Plasmas, Fluids, and Related Interdisciplinary Topics*, 72, 021308. <https://doi.org/10.1103/physreve.72.021308>
- Endo, N., Taniguchi, K., & Katsuki, A. (2004). Observation of the whole process of interaction between barchans by flume experiments. *Geophysical Research Letters*, 31, L12503. <https://doi.org/10.1029/2004gl020168>
- Florez, J. E. C., & Franklin, E. M. (2016). The formation and migration of sand ripples in closed conduits: Experiments with turbulent water flows. *Experimental Thermal and Fluid Science*, 71, 95–102. <https://doi.org/10.1016/j.expthermflusci.2015.10.017>
- Fourrière, A., Claudin, P., & Andreotti, B. (2010). Bedforms in a turbulent stream: Formation of ripples by primary linear instability and of dunes by nonlinear pattern coarsening. *Journal of Fluid Mechanics*, 649, 287–328. <https://doi.org/10.1017/s0022112009993466>
- Fredsoe, J. (1974). On the development of dunes in erodible channels. *Journal of Fluid Mechanics*, 64, 1–16.
- Gadal, C., Narteau, C., du Pont, S. C., Rozier, O., & Claudin, P. (2018). Incipient bedforms in a bidirectional wind regime. *Journal of Fluid Mechanics*, 862, 490–516.
- Gao, X., Narteau, C., & Rozier, O. (2015). Development and steady states of transverse dunes: A numerical analysis of dune pattern coarsening and giant dunes. *Journal of Geophysical Research: Earth Surface*, 120, 2200–2219. <https://doi.org/10.1002/2015jg003549>
- Groh, C., Rehberg, I., & Kruelle, C. A. (2009). How attractive is a barchan dune? *New Journal of Physics*, 11, 023014. <https://doi.org/10.1088/1367-2630/11/2/023014>
- Guy, H. P., Simons, D. B., & Richardson, E. V. (1966). *Summary of alluvial channel data from flume experiments, 1956 – 61* (pp. 462–I). USGS Prof. Pap.
- Hardy, R. J., Best, J. L., Marjoribanks, T. I., Parsons, D. R., & Ashworth, P. J. (2021). The influence of three-dimensional topography on turbulent flow structures over dunes in unidirectional flows. *Journal of Geophysical Research: Earth Surface*, 126. <https://doi.org/10.1029/2021jg006121>
- Hersen, P. (2005). Flow effects on the morphology and dynamics of aeolian and subaqueous barchan dunes. *Journal of Geophysical Research*, 110, F04S07. <https://doi.org/10.1029/2004jg000185>
- Hurther, D., Thorne, P. D., Bricault, M., Lemmin, U., & Barnoud, J.-M. (2011). A multi-frequency Acoustic Concentration and Velocity Profiler (ACVP) for boundary layer measurements of fine-scale flow and sediment transport processes. *Coastal Engineering*, 58, 594–605. <https://doi.org/10.1016/j.coastaleng.2011.01.006>
- Jackson, P. S., & Hunt, J. C. R. (1975). Turbulent wind flow over a low hill. *Quarterly Journal of the Royal Meteorological Society*, 101, 929–955. <https://doi.org/10.1002/qj.49710143015>
- Jerolmack, D. J., & Mohrig, D. (2005). A uniflow model for subaqueous bed form dynamics. *Water Resources Research*, 41, W12421. <https://doi.org/10.1029/2005wr004329>
- Ji, Z., & Mendoza, C. (1997). Weakly nonlinear stability analysis for dune formation. *Journal of Hydraulic Engineering*, 123, 979–985. [https://doi.org/10.1061/\(asce\)0733-9429\(1997\)123:11\(979\)](https://doi.org/10.1061/(asce)0733-9429(1997)123:11(979))
- Kleinhans, M. G., Wilbers, A. W. E., Swaaf, A. D., & Berg, J. H. V. D. (2002). Sediment supply-limited bedforms in sand-gravel bed rivers. *Journal of Sedimentary Research*, 72, 629–640. <https://doi.org/10.1306/030702720629>
- Krishnappan, B. G. (1993). Rotating circular flume. *Journal of Hydraulic Engineering*, 119, 758–767. [https://doi.org/10.1061/\(asce\)0733-9429\(1993\)119:6\(758\)](https://doi.org/10.1061/(asce)0733-9429(1993)119:6(758))
- Kroy, K., Sauermaun, G., & Herrmann, H. J. (2002). Minimal model for sand dunes. *Physical Review Letters*, 88, 054301. <https://doi.org/10.1103/physrevlett.88.054301>
- Kunii, D., & Levenspeil, O. (1968). *Fluidisation engineering*. John Wiley.
- Lajeunesse, E., Malverti, L., & Charru, F. (2010). Bed load transport in turbulent flow at the grain scale: Experiments and modeling. *Journal of Geophysical Research*, 115, F04001. <https://doi.org/10.1029/2009jg001628>
- Lavelle, W. J., & Mojfeld, H. O. (1987). Do critical stress for incipient motion and erosion really exist? *Journal of Hydraulic Engineering*, 113, 370–385. [https://doi.org/10.1061/\(asce\)0733-9429\(1987\)113:3\(370\)](https://doi.org/10.1061/(asce)0733-9429(1987)113:3(370))
- Lefebvre, A., Paarlberg, A. J., & Winter, C. (2013). Flow separation and shear stress over angle-of-repose bed forms: A numerical investigation. *Water Resources Research*, 50, 986–1005.
- Lorenz, R. D., & Zimbelman, J. R. (2014). *Dune worlds, how windblown sand shapes planetary landscapes*. Springer Praxis Books.
- Lü, P., Narteau, C., Dong, Z., Claudin, P., Rodriguez, S., An, Z., & du Pont, S. C. (2021). Direct validation of dune instability theory. *Proceedings of the National Academy of Sciences of the United States of America*, 118. <https://doi.org/10.1073/pnas.2024105118>
- Maddux, T. B., Nelson, J. M., & Mclean, S. R. (2003). Turbulent flow over three-dimensional dunes: 2. Fluid and BES stresses. *Journal of Geophysical Research*, 108. <https://doi.org/10.1029/2003jg000018>
- Mantz, P. A. (1978). Bedforms produced by fine, cohesionless, granular and flakey sediments under subcritical water flows. *Sedimentology*, 25, 83–103. <https://doi.org/10.1111/j.1365-3091.1978.tb00302.x>
- Martin, R. L., & Jerolmack, D. J. (2013). Origin of hysteresis in bed form response to unsteady flows. *Water Resources Research*, 49, 1314–1333. <https://doi.org/10.1002/wrcr.20093>
- Mcculloch, D. S., & Janda, R. J. (1964). Subaqueous river channel barchan dunes. *Journal of Sedimentary Petrology*, 34, 694.
- Meyer-Peter, E., & Müller, R. (1948). *Formulas for bed-load transport*. Proc., 2nd meeting IAHR (pp. 39–64).
- Mouilleron, H., Charru, F., & Eiff, O. (2009). Inside the moving layer of a sheared granular bed. *Journal of Fluid Mechanics*, 628, 229–239. <https://doi.org/10.1017/s0022112009006636>
- Naqshband, S., Hoitink, A. J. F., McElroy, B., Hurther, D., & Hulscher, S. J. M. H. (2017). A sharp view on river dune transition to upper stage plane bed. *Geophysical Research Letters*, 44, 11437–11444. <https://doi.org/10.1002/2017gl075906>
- Naqshband, S., Hurther, D., Giri, S., Bradley, R. W., Kostaschuk, R. A., Venditti, J. G., & Hoitink, A. J. F. (2021). The influence of slipface angle on fluvial dune growth. *Journal of Geophysical Research: Earth Surface*, 126. <https://doi.org/10.1029/2020jg005959>
- Naqshband, S., Ribberink, J. S., Hurther, D., & Hulscher, S. J. M. H. (2014). Bed load and suspended load contributions to migrating sand dunes in equilibrium. *Journal of Geophysical Research: Earth Surface*, 119, 1043–1063. <https://doi.org/10.1002/2013jg003043>
- Nikora, V. I., & Hicks, D. M. (1997). Scaling relationships for sand wave development in unidirectional flow. *Journal of Hydraulic Engineering*, 123. [https://doi.org/10.1061/\(asce\)0733-9429\(1997\)123:12\(1152\)](https://doi.org/10.1061/(asce)0733-9429(1997)123:12(1152))
- Pächt, T., Clark, A. H., Valyrakis, M., & Durán, O. (2020). The physics of sediment transport initiation, cessation, and entrainment across aeolian and fluvial environments. *Reviews of Geophysics*, 58. <https://doi.org/10.1029/2019rg000679>
- Pächt, T., & Durán, O. (2020). Unification of aeolian and fluvial sediment transport rate from granular physics. *Physical Review Letters*, 124. <https://doi.org/10.1103/physrevlett.124.168001>

- Paintal, A. S. (1971). Concept of critical shear stress in loose boundary open channels. *Journal of Hydraulic Research*, 9. <https://doi.org/10.1080/00221687109500339>
- Parteli, E. J. R., Andrade, J. S., Jr, & Hermann, H. J. (2011). Transverse instability of dunes. *Physical Review Letters*, 107. <https://doi.org/10.1103/physrevlett.107.188001>
- Petersen, O., & Krishnappan, B. G. (1994). Measurement and analysis of flow characteristics in a rotating circular flume. *Journal of Hydraulic Research*, 32, 483–494. <https://doi.org/10.1080/00221686.1994.9728351>
- Reesink, A. J. H., Parsons, D. R., Ashworth, P. J., Best, J. L., Hardy, R. J., Murphy, B. J., & Unsworth, C. (2018). The adaptation of dunes to changes in river flow. *Earth-Science Reviews*, 185, 1065–1087. <https://doi.org/10.1016/j.earscirev.2018.09.002>
- Reffet, E., du Pont, S. C., Hersen, P., & Douady, S. (2010). Formation and stability of transverse and longitudinal sand dunes. *Geology*, 38, 491–494. <https://doi.org/10.1130/g30894.1>
- Robert, A., & Uhlman, W. (2000). An experimental study on the ripple-dune transition. *Earth Surface Processes and Landforms*, 26, 615–629.
- Rousseaux, G., Stegner, A., & Wesfreid, J. E. (2004). Wavelength selection of rolling-grain ripples in the laboratory. *Physical Review E*, 69. <https://doi.org/10.1103/physreve.69.031307>
- Salevan, J. C., Clark, A. H., Shattuck, M. D., O'Hern, C. S., & Ouellette, N. T. (2017). Determining the onset of hydrodynamic erosion in turbulent flow. *Phys. Rev. Fluids*, 2, 114302. <https://doi.org/10.1103/physrevfluids.2.114302>
- Shields, A. (1936). *Anwendung der aehnlichkeitsmechanik und der turbulenzforschung auf die gescheibebewegung (Unpublished doctoral dissertation)*.
- Skulovich, O., Cofalla, C., Ganal, C., Schüttrumpf, H., & Ostfeld, A. (2017). Modelling of resuspension due to fish activity: Mathematical modeling and annular flume experiments. *International Journal of Sediment Research*, 32, 421–431. <https://doi.org/10.1016/j.ijsrc.2017.07.003>
- Southard, J. B. (1991). Experimental determination of bed-form stability. *Annual Review of Earth and Planetary Sciences*, 19, 423–455. <https://doi.org/10.1146/annurev.ea.19.050191.002231>
- Sumner, E. J., Amy, L. A., & Talling, P. J. (2008). Deposit structure and processes of sand deposition from decelerating sediment suspensions. *Journal of Sedimentary Research*, 78, 529–547. <https://doi.org/10.2110/jsr.2008.062>
- Swanson, T., Mohrig, D., & Liang, G. K. M. (2017). A surface model for aeolian dune topography. *Mathematical Geosciences*, 49, 635–655. <https://doi.org/10.1007/s11004-016-9654-x>
- Telfer, M. W., Parteli, E. J. R., Radebaugh, J., Beyer, R. A., Bertrand, T., Forget, F., et al. (2018). Dunes on Pluto. *Science*, 360, 992–997. <https://doi.org/10.1126/science.aao2975>
- Thompson, C. E. L., Amos, C. L., Lecouturier, M., & Jones, T. E. R. (2004). Flow deceleration as a method of determining drag coefficient over roughened flat beds. *Journal of Geophysical Research*, 109, C03001. <https://doi.org/10.1029/2001jc001262>
- Tuijinder, A. P., Ribberink, J. S., & Hulscher, S. J. M. H. (2009). An experimental study into the geometry of supply-limited dunes. *Sedimentology*, 56, 1713–1727.
- Valance, A. (2011). Nonlinear sand bedform dynamics in a viscous flow. *Physical Review E - Statistical Physics, Plasmas, Fluids, and Related Interdisciplinary Topics*, 83, 036304. <https://doi.org/10.1103/physreve.83.036304>
- Venditti, J. G. (2007). Turbulent flow and drag over fixed two- and three-dimensional dunes. *Journal of Geophysical Research*, 112, F04008. <https://doi.org/10.1029/2006jf000650>
- Venditti, J. G., Church, M. A., & Bennett, S. J. (2005a). Bed form initiation from a flat sand bed. *Journal of Geophysical Research*, 110, F01009. <https://doi.org/10.1029/2004jf000149>
- Venditti, J. G., Church, M. A., & Bennett, S. J. (2005b). On the transition between 2D and 3D dunes. *Sedimentology*, 52, 1343–1359. <https://doi.org/10.1111/j.1365-3091.2005.00748.x>
- von Kármán, T. (1930). *Nachrichten von der Gesellschaft der Wissenschaften zu Göttingen, Fachgruppe 1 (Mathematik). Mechanische Ähnlichkeit und Turbulenz* (pp. 58–76).
- Wei, H., Ya-kun, L., Hua-lin, W., & Yuan-yang, W. (2017). The incipient motion features of sediment from Yangtze estuary: Annular flume experiments. *Scientific Reports*, 7, 13285. 620–631. <https://doi.org/10.1038/s41598-017-13651-2>
- Weller, H. G., & Tabor, G. (1998). A tensorial approach to computational continuum mechanics using object-oriented techniques. *Computers in Physics*, 12. <https://doi.org/10.1063/1.168744>
- Widdows, J., Friend, P. L., Bale, A. J., Brinsley, M. D., Pope, N. D., & Thompson, C. E. L. (2007). Inter-comparison between five devices for determining erodability of intertidal sediments. *Continental Shelf Research*, 27, 1174–1189. <https://doi.org/10.1016/j.csr.2005.10.006>
- Wierschem, A., Groh, C., Rehberg, I., Aksel, N., & Kruehle, C. A. (2008). Ripple formation in weakly turbulent flow. *European Physical Journal E*, 25, 213–221. <https://doi.org/10.1140/epje/i2007-10282-4>
- Yang, S., Im, I., Hwang, K., Cho, Y., & Ryu, H. (2015). A numerical study on optimal rotation ratio and bottom shear stress in the counter-rotation mode of an annular flume. *Journal of Hydro-environment Research*, 9, 473–481. <https://doi.org/10.1016/j.jher.2015.02.002>
- Yang, Z., Baptista, A., & Darland, J. (2000). Numerical modeling of flow characteristics in a rotating annular flume. *Dynamics of Atmospheres and Oceans*, 31, 271–294. [https://doi.org/10.1016/s0377-0265\(99\)00037-8](https://doi.org/10.1016/s0377-0265(99)00037-8)

## Reference From the Supporting Information

- Courant, R., Friedrichs, K., & Lewy, H. (1928). Über die partiellen Differenzgleichungen der mathematischen Physik. *Mathematische Annalen*, 100, 32–74. <https://doi.org/10.1007/bf01448839>